Progress In Electromagnetics Research C, Vol. 61, 115–125, 2016

A Dual-Band Low-Profile Metasurface-Enabled Wearable Antenna for WLAN Devices

Helin Yang[1, *], Wang Yao[1], Yuanyuan Yi[2], Xiaojun Huang[1, 3], Song Wu[1], and Boxun Xiao[2]

Abstract—This paper presents a compact, low-profile, wearable dual-band antenna operating in the Wireless WLAN band of 5.15 ∼ 5.25 GHz and 5.72 ∼ 5.83 GHz. The proposed antenna is composed of a planar monopole and underneath three by three array arrangement of Jerusalem Cross (JC) structure metasurface. The simulated results show that the integrated antenna express 4.09% and 4.14% impendence bandwidths, increased gain up to 7.9 dB and 8.2 dB, front to back (FB) ratio achieved to 20 dB and 18 dB at the two frequencies, respectively. The measured results agree well with simulations. In addition, the metasurface not only is equivalent to a ground plane for isolation, but also acts as the main radiator, which enables a great reduction in the specific absorption rate (SAR). Furthermore, because of a compact solution, the proposed integrated antenna can be a promising device for various wearable systems.

1. INTRODUCTION

The research of wearable computing systems has experienced rapid development over the past decade due to their great potential applications such as health monitoring, wireless communication and other intelligent terminals [1–3]. As one of the key components in the communication system, wearable antennas have received much attention in both academia and industry since their unconventional operating environment is in extremely close proximity to the human body [4]. In this case, the loading of lossy human tissue makes the design of a high radiation efficiency antenna challenging when it is also desirable for it to possess light-weight and low-profile characteristics [5, 6]. Simultaneously, the impact of a wearable antenna on human tissue, characterized by the specific absorption rate (SAR), also needs to be minimized. The Planar Inverted-F Antenna (PIFA) was used to be an ideal scheme for the wearable antenna design since it has the promising characteristics such as compactness, flexibility and multi-frequency [7, 8]; however, the performance of SAR was substandard, and the impendence was easily be changed when loading by the human tissue. Alternatively, the Electromagnetic Band-Gap (EBG) and Artificial Magnetic Conductor (AMC) ground plane were introduced in the wearable antenna design [9, 10]; such substrates can isolate the radiation field and body tissue, decreased the SAR dramatically, while these solutions still suffer from relatively large footprints, over-thick or low front to back (FB) ratios.

Metamaterials are artificial materials with unusual electromagnetic responses that are not possessed by natural materials [11, 12]. In the past decades, researchers have engaged in planar metamaterials composed of subwavelength periodic resonant or non-resonant unit cells [13], which are also called as metasurfaces. Some important applications of metasurfaces are anomalous refraction or reflection [14],

Received 28 September 2015, Accepted 29 December 2015, Scheduled 12 January 2016

* Corresponding author: Helin Yang (emyang@mail.ccnu.edu.cn).

[1] College of Physical Science and Technology, Central China Normal University, Wuhan 430079, China. [2] Engineering Geophysical Research Center, Yangtze University, Jingzhou 434023, China. [3] College of Physics and Electrical Engineering, Kashgar University, Kashgar 844000, China.

surface-wave conversion, and polarization transformation, and they have also led to a wide range of applications in the antenna and propagation fields [15]. Metasurfaces not only are used to improve the properties of antennas including bandwidth and gain, but also can eliminate the aforementioned drawbacks. In order to ensure the antenna to work in a proper frequency, the metasurface must have the function of frequency selection. Frequency Selective Surface (FSS) based on Jerusalem Cross (JC) structure has been applied in the design of microwave and Radio Frequency (RF) systems, such as filters, polarizers and couplers [16, 17]. JCs offer a miniaturized structure over the conventional square-patch based FSS suggested originally by Sievenpiper et al. [18]. Compared to the traditional Series-Resonant Grids, JC structures are more flexible on frequency selection and more miniaturized on size [19]. Hence, this structure was selected as candidate for the targeted application which requires the metasurface to follow certain properties in the target band.

In this paper, we present a dual-band low-profile printed monopole antenna integrated with a metasurface ground plane based on a miniaturized Jerusalem Cross (JC) structure. It functions in the Wireless Local Area Networks (WLAN) band of 5.15 $\sim$ 5.25 GHz and 5.72 $\sim$ 5.83 GHz, respectively, following the IEEE 802.11a standard [20]. In Section 2, we present the design of the antenna and metasurface ground plane. The results of three kinds of antenna are presented in Section 3, and the effects of human body loading on the antennas are also studied in this section. It has been proved that the metasurface can reduce the peak SAR value considerably. Finally, conclusions are given in Section 4.

2. THE DESIGN OF ANTENNA AND METASURFACE

The antenna consists of two components, a planar monopole on the top and a custom-designed metasurface at the bottom. The top view of the planar monopole is demonstrated in Figure 1. The planar monopole is fed by a Coplanar Waveguide (CPW), and the patch is printed on the top surface of a 36 mm by 30 mm Rogers RO4003 substrate with a dielectric constant of 3.38 and loss tangent of 0.0027. The thickness of the substrate is only 0.305 mm which is thinner and lighter than previous schemes. The dimensions are $L_1 = 32$ mm, $L_2 = 20$ mm, $L_3 = 11$ mm, $L_4 = 5.5$ mm, $W_1 = 24$ mm, $W_2 = 10$ mm, $W_3 = 1.6$ mm, $W_4 = 0.6$ mm.

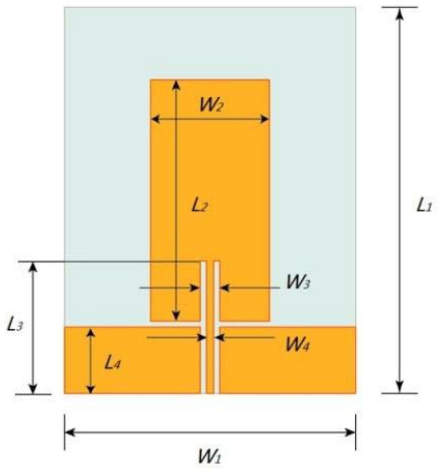

Figure 1. Top view of the monopole.

The substrate of metasurface has the same material and thickness as the planar monopole. The unit cell configuration on the surface is based on the shape of JC. The metasurface comprises 3×3 unit cells, and the bottom layer is covered by copper, as shown in Figure 2. The dimensions are $a = 14.4$ mm, $b = 13.4$ mm, $c = 8.8$ mm, $d = 4.8$ mm, $e = 1.4$ mm. The monopole, as an efficient excitation, parallels to the metasurface.

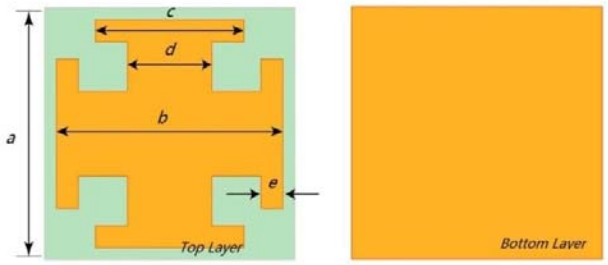

Figure 2. Geometry and dimensions of the JC based metasurface.

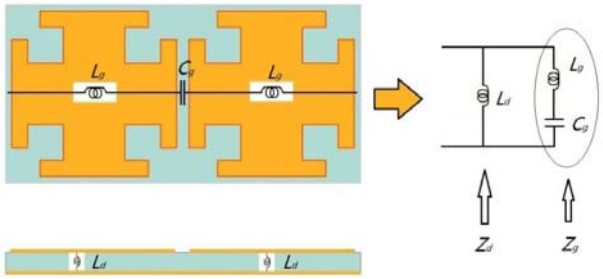

Figure 3. Equivalent circuit of JC-based metasurface.

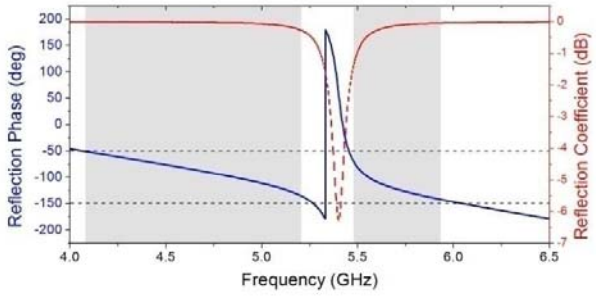

Figure 4. Reflection phase and coefficient for the JC based metasurface.

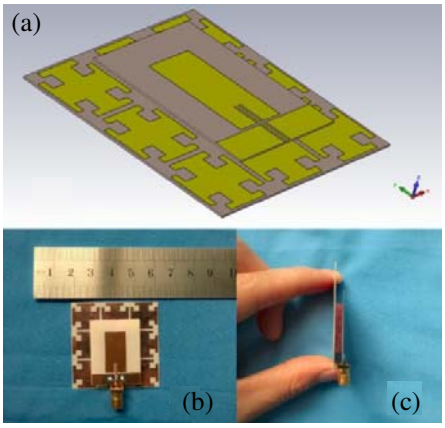

Figure 5. (a) Configuration of the integrated planar antenna, (b) front and (c) side view of the integrated planar antenna.

We deal with the modeling and characterization of the JC structure metasurface composed of periodic resonant LC cells [21]. A circuit model for the JC structures is depicted in Figure 3. To make the metasurface operate at the proper band, the geometrical dimensions of the metasurface were tuned to yield a zero reflection phase around 5.5 GHz and ensure the $-90°$ reflection phase to occur at the target bands. It is evident that the structure can be miniaturized by increasing one of the following parameters: the grid inductance L_g, dielectric inductance L_d, and grid capacitance C_g [22, 23]. Obviously, increasing L_d leads to a higher profile structure which is not preferred for the considered application. Resonant frequency of the structure can be expressed as

$$f = \frac{1}{2\pi\sqrt{(L_g + L_d)C_g}} \tag{1}$$

Once defining the geometry of the JC structure, we will have the values of corresponding inductances and capacitances, and the reflection and transmission characteristics can then be visualized automatically [24]. For characterization, we used the CST Microwave Studio to analyze the reflection behavior, in which the finite integration technique was applied. The program was simulated with appropriate boundary conditions, as a unit cell in the x and y directions, and open (add space) in the z direction. Electromagnetic waves were normal incident on the surface of the structure. Figure 4 shows the simulated results of the reflection phase and reflection coefficient profiles of the proposed JC structures. The gray areas are the range $-90° \pm 45°$ reflection phase region. The frequency bands $4.1 \sim 5.2$ GHz and $5.5 \sim 5.9$ GHz are the target frequency where we want to achieve good impendence matching for the proposed antenna.

3. RESULTS AND DISCUSSIONS

Configuration of the integrated metasurface-enabled antenna is shown in Figure 5(a). The metasurface and monopole were first fabricated separately using standard print circuit broad (PCB) etching. A foam spacer with the prescribed thickness was then added in the two components, as shown in Figures 5(b) and 5(c).

3.1. S-Parameters

The simulated impedance performance of the monopole in free space is illustrated in Figure 6(a). The monopole alone shows a poor impedance match through the entire band, and the reflectance is higher than -10 dB. The monopole placed above a metallic sheet was also simulated, which achieved a single impedance matched band with S_{11} lower than -10 dB. It has also been demonstrated that the integrated antennas consisting of a radiator backed by a metasurface ground plane working at operational band around 0° or $+90^\circ$ reflection phase frequency [25], while the frequency bandwidth of 0° or $+90^\circ$ reflection phase would be extremely narrow when the thickness of ground plane was only 0.305 mm. However, the metasurface with -90° reflection phase can achieve a wider and dual-band antenna, thus the metasurface with -90° reflection phase was adopted in the proposed design (see in Figure 4).

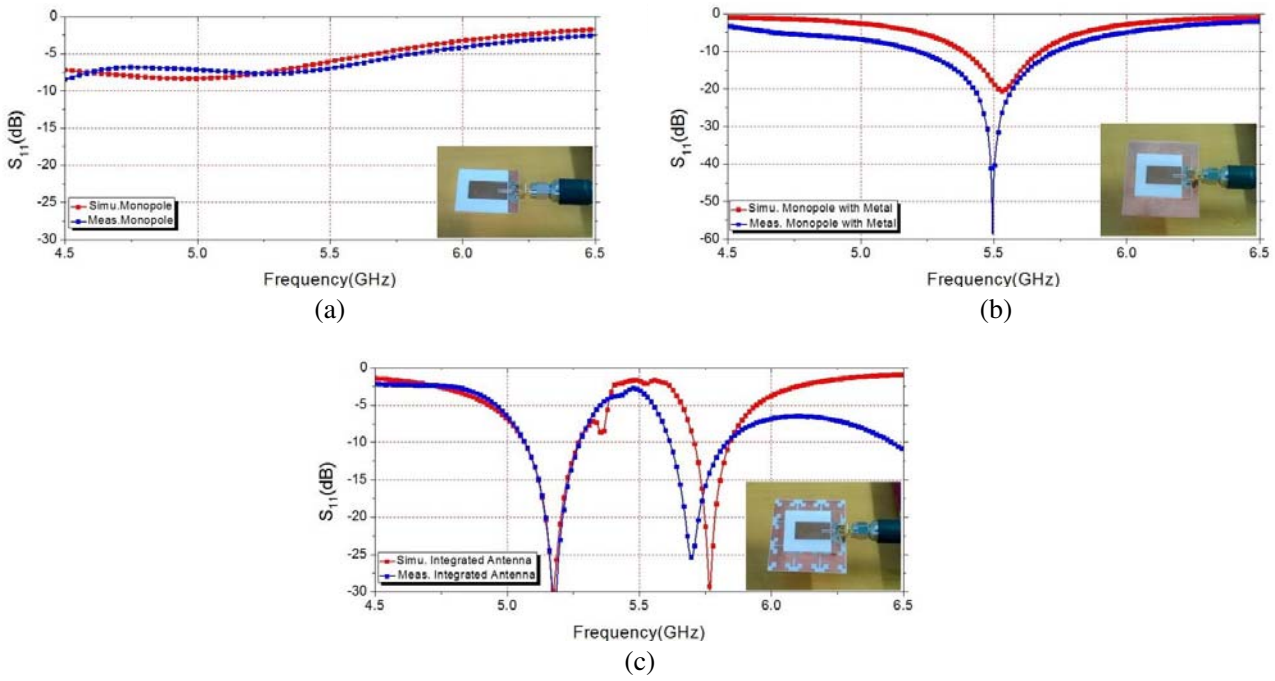

Figure 6. Simulated and measured S_{11} of (a) the monopole alone in free space, (b) the monopole above a PEC ground plane, (c) the integrated metasurface-enabled antenna.

The monopole alone in the free space has a dipole-like pattern in E-plane and an omnidirectional pattern in H-plane. When the monopole is integrated with metal plate, most of the energy is radiated towards the $+z$ half space with a half-power beamwidth (HPBW) about 60° and 75° in E-plane and H-plane. The integrated antenna exhibits a -10 dB impedance bandwidth at $5.38 \sim 5.67$ GHz, as shown in Figure 6(b) and Figures 7(c), (d). When the monopole is integrated with the designed metasurface, depicted in Figure 6(c), most of the energy is radiated towards the $+z$ half space as well. The integrated antenna exhibits a couple of -10 dB impedance bandwidths at $5.06 \sim 5.27$ GHz and $5.68 \sim 5.84$ GHz. The HPBW in the lower band are about 65° and 75° in the E-plane and H-plane and about 60° and 75° in the higher band, as shown in Figures 7(e) and 7(f).

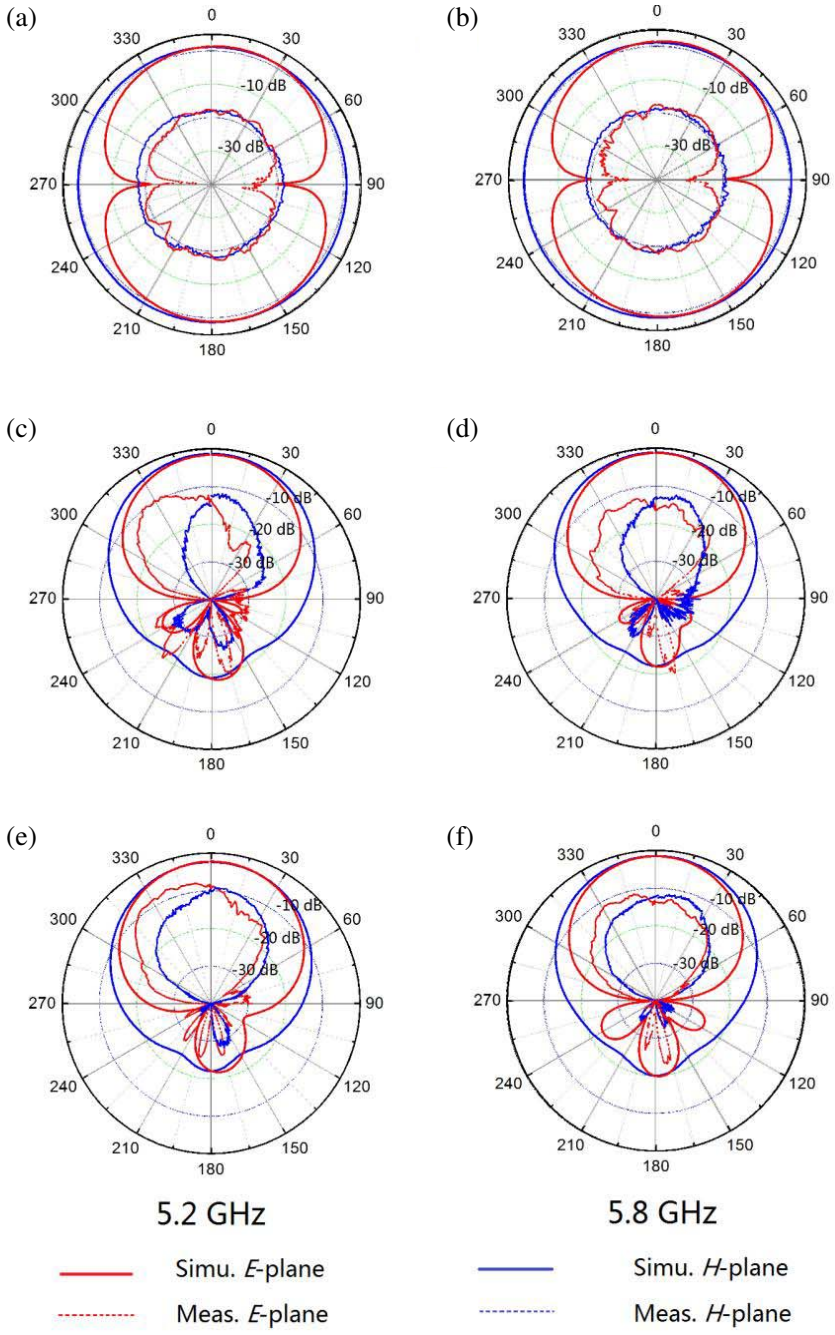

Figure 7. Simulated and measured E-plane and H-plane radiation pattern of (a), (b) the monopole, (c), (d) integrated PEC-enabled antenna and (e), (f) the metasurface-enabled antenna at two different resonant frequencies.

To get a better understanding of the two sufficient wide operational frequency bands, the metasurface with $-90°$ reflection phase was utilized, which acted as a capacitive surface in the two operational bands [26]. Since the monopole alone is operated at the frequency above its fundamental resonant mode, its input impedance is inductive. When the monopole is loaded by the capacitive impedance surface which can store more magnetic energy, the reactance of the integrated antenna can be suppressed [25], thus achieving a good impedance match.

The surface current distributions of the monopole and integrated antenna at the frequency of

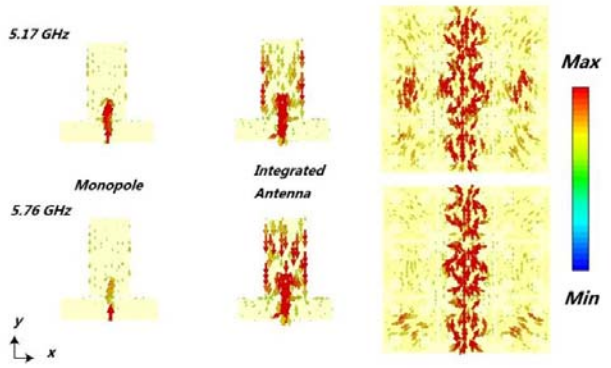

Figure 8. Simulated surface current of the monopole and metasurface at 5.2 GHz and 5.5 GHz.

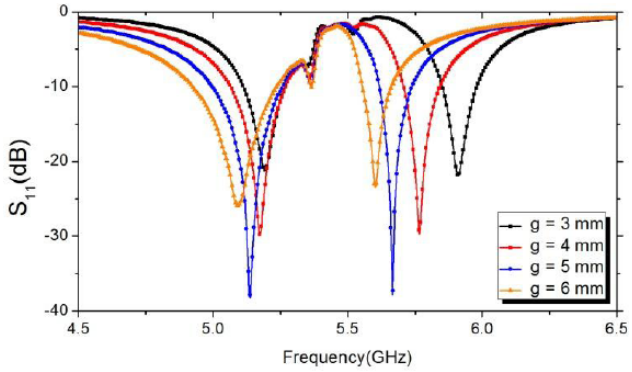

Figure 9. Simulated S_{11} of the proposed antenna with different gaps between the monopole and metasurface.

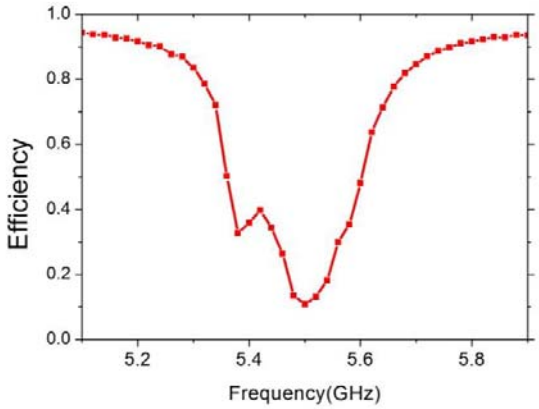

Figure 10. Simulated efficiency of the proposed antenna.

5.17 GHz and 5.76 GHz are illustrated in Figure 8. When the monopole is simulated alone, the current distributions are mainly concentrated on the feeding line. The magnetic resonance will occur between the monopole and metasurface when they are close to each other since the current distributions are both on the monopole and metasurface. It furthermore proves that the metasurface acts as a main radiator in the antenna and significantly improves the radiation characteristics of the proposed antenna.

The effect of the gap between the monopole and metasurface is also explored. The simulated S-parameter of the gap varied from 3 mm to 6 mm is exhibited in Figure 9. With widening of the gap, the bandwidth at the first band (below 5.5 GHz) was broadened, and the second band (above 5.5 GHz) was redshifted. The efficiency of the integrated antenna would be decreased when the frequency band was close to 5.5 GHz. Therefore, the thickness of 4 mm was selected as the optimal choice, and the two bandwidths are wide enough. The total thickness of the integrated antenna is only 4.6 mm which agrees well with the purpose of low-profile as well. The simulated efficiency of the integrated antenna with 4 mm gap is shown in Figure 10. The efficiency in the WLAN band is around 0.9, indicating that the proposed antenna is well designed with high efficiency.

3.2. Gain and FB Ratio

The gain and front to back (FB) ratio are desirable characteristics to identify whether the antenna has the potential for wearable applications. The monopole alone has a simulated gain of 2.5 dB whereas the integrated antenna has a simulated gain of 7.9 dB at 5.2 GHz and 8.2 dB at 5.8 GHz, as the gray areas shown in Figure 11(a). In terms of FB ratio, while the value of the monopole approaches zero, the

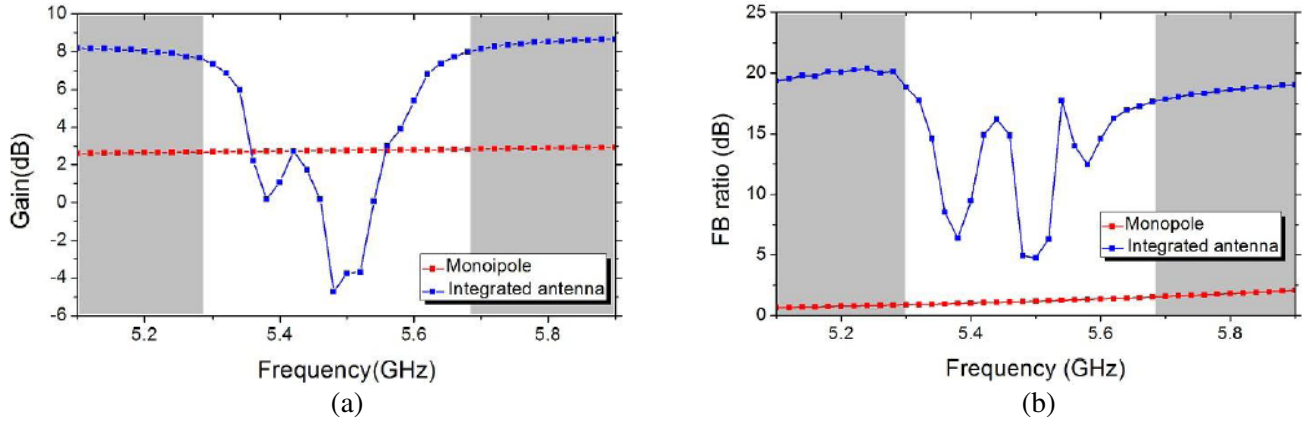

Figure 11. (a) Simulated gain of the monopole alone and the integrated antenna, (b) simulated FB ratio of the monopole alone and the integrated antenna.

integrated antenna has a simulated FB ratio around 20 dB and 18 dB at the working frequency band of 5.15–5.25 GHz and 5.72–5.83 GHz, respectively, as the gray areas shown in Figure 11(b). Such a high FB ratio indicates that very little energy will be radiated into the tissue when the antenna is placed on the human body. This property can reduce the SAR value and make the antenna more stable to the loading effects of the human body, both of which are essential characteristics for wearable applications.

3.3. Experimental Results

In measurement, an Agilent E8362B network analyzer was used to characterize the S_{11} of both the monopole and the integrated metasurface-enabled antenna in free space. The measured S_{11} of the integrated antenna has two relative bandwidths of 4.07% at 5.06 $\sim$ 5.27 GHz and 4.16% at 5.60 $\sim$ 5.84 GHz, as shown in Figure 6. Good agreement can be found between simulated and measured results. Remarkably, the test result of the band above 5.5 GHz has a slight difference from the simulations. Discrepancy comes from the deviation of the parameter of the material between the simulation and the test. For example, dielectric coefficient changes as the frequency increases while in simulation, the coefficient will be a constant.

The far-field radiation patterns of E- and H-planes were measured at 5.2 GHz and 5.8 GHz, which are depicted in Figure 7. Figures 7(a), (b) indicate the printed monopole which retains a reasonable omnidirectional radiation patterns at resonance. When the monopole is integrated with metal plate, the radiation patterns turn unidirectional, shown in Figures 7(c), (d). However, the measured HPBWs are too narrow to meet the design specification. Then, the metal plate was replaced by the proposed

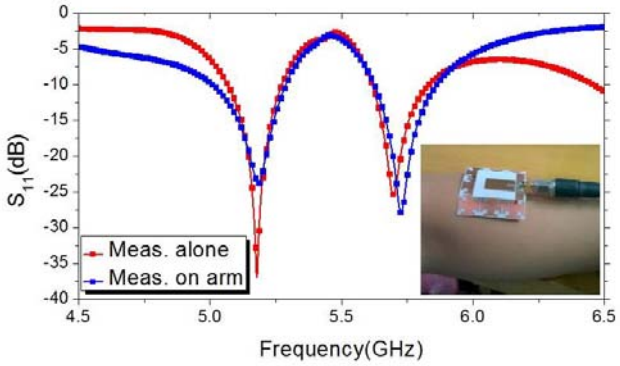

Figure 12. Measured S_{11} of the integrated antenna placed on arm compared with the antenna measured alone.

metasurface; the HPBWs turn broader; the radiation patterns in both E- and H-planes agree well with the simulated results, shown in Figures 7(e), (f).

In further research to prove that the integrated antenna has a good impendence matching with the body tissue, we measured the S_{11} of the antenna placed on arm. As shown in Figure 12, a very stable S_{11} is maintained for the case that the antenna is directly placed on arm, which basically obeys the result of the antenna measured in the free space.

3.4. SAR Evaluation

SAR is a standard measure used to evaluate the electromagnetic power deposition in the human tissues. According to the guidelines specified by the Federal Communication Commission (FCC), SAR values must not exceed the exposure limit which is 1.6 W/kg averaged over 1 g of tissue [27]. The SAR value is related to the applied input power by

$$\mathrm{SAR} = \sigma |E|^2 / \rho \tag{2}$$

where σ is the conductivity of the tissue in S/m, $\mathbf{E}$ the electric field in V/m, and ρ the mass density of the tissue in kg/m^3. As a benchmark, a 100 mW power accepted by the antenna is chosen to evaluate and compare the SAR performance of the monopole and the proposed integrated antenna.

The configurations are shown in Figure 13, where the antennas are placed on a multilayer human tissue model. The skin, fat, muscle, and bone layers have thickness values of 2 mm, 5 mm, 20 mm, and 13 mm, respectively [28, 29]. For each layer, typical permittivity, conductivity, and mass density values are reported in the literature [30], as listed in Table 1.

The simulated averaged SAR is shown in Figure 14 and Table 2, and variable d represents the distance between simulated antenna and the tissue model. The proposed monopole and integrated antenna operated near the tissue model with four different distances, respectively. As shown in the table, for the considered input power, the monopole generates maximum 1 g averaged SAR value of about 6.6 W/kg at 5.2 GHz and 11.7 W/kg at 5.8 GHz even at a distance of 4 mm away from the tissue model, which has surpassed the FCC standard. For the integrated antenna, the maximum 1 g averaged SAR value drops to 0.0646 W/kg at 5.2 GHz and 0.0268 W/kg at 5.8 GHz only at a distance of 4 mm away from the tissue model, as can be found in Table 2. Figure 14 shows the great disparity of SAR

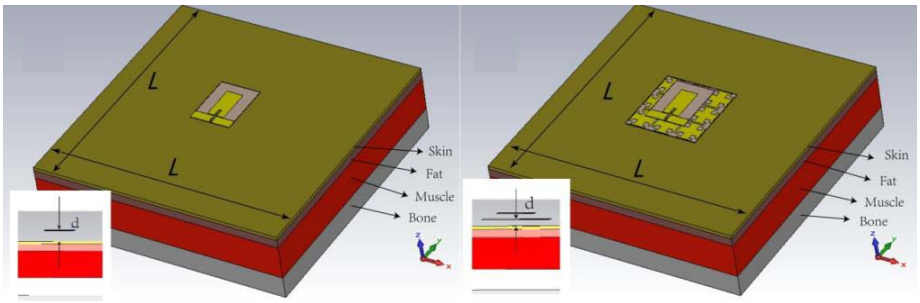

(a) (b)

Figure 13. Configurations of (a) the monopole antenna and (b) the integrated antenna when place on a multilayer tissue model $L = 150$ mm.

Table 1. Material properties of the multilayer human tissue model.

	Skin	Fat	Muscle	Bone
ε_r	37.95	5.27	52.67	18.49
σ (S/m)	1.49	0.11	1.77	0.82
Density (kg/mm^3)	1001	900	1006	1008
Thickness (mm)	2	5	20	13

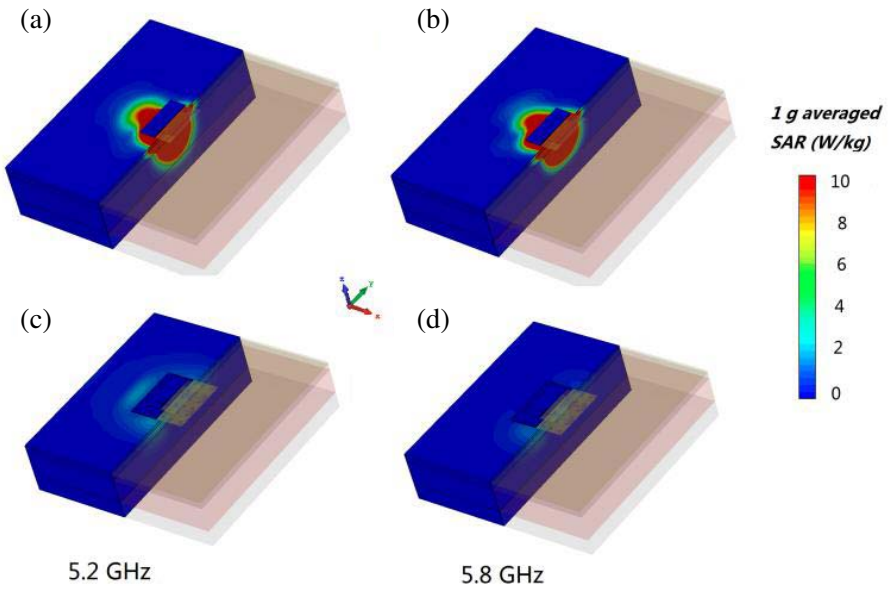

Figure 14. Simulated averaged SAR value for (a), (b) the monopole and (c), (d) the integrated antenna at 2 mm away from the tissue model.

Table 2. Maximum 1 g averaged SAR value for the monopole and the integrated antenna (units: W/kg).

($f = 5.2$ GHz)

d	1 mm	2 mm	3 mm	4 mm
Monopole	6.62	13.1	8.56	6.60
Integrated Antenna	0.0646	0.0449	0.0341	0.0176

($f = 5.8$ GHz)

d	1 mm	2 mm	3 mm	4 mm
Monopole	10.3	25.3	15.8	11.7
Integrated Antenna	0.0258	0.0315	0.0176	0.0091

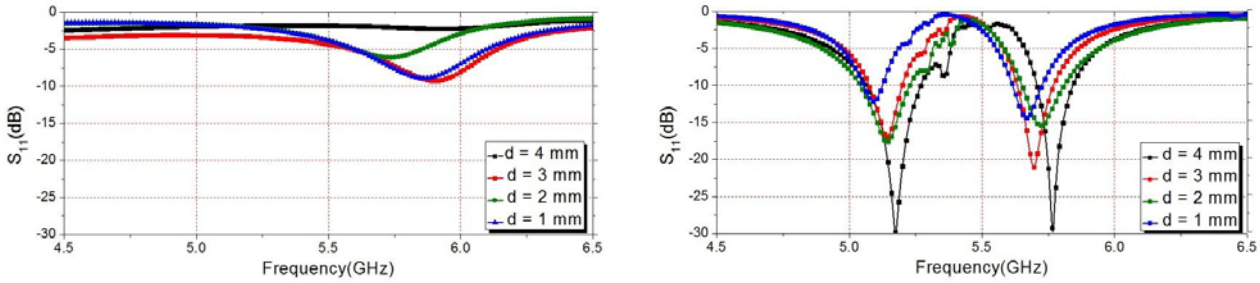

Figure 15. Simulated S_{11} for (a) the monopole and (b) the integrated antenna at different distances away from the tissue model.

values between the monopole and the integrated antenna, which have strongly proved that the adoption of metasurface has the effect of reducing SAR dramatically and decreases the injury of humans body from electromagnetic radiations.

In addition, we investigate the effects of human body by placing the monopole and integrated antenna on the designed tissue model. The distance between the antenna and tissue model was varied from 1 mm to 4 mm. The monopole always shows a poor impendence matching at the Wireless WLAN band of $5.15 \sim 5.25$ GHz and $5.72 \sim 5.83$ GHz, as displayed in Figures 15(a) and (b), while the integrated metasurface-enabled antenna shows a steady -10 dB bandwidth as it functions alone.

4. CONCLUSION

In conclusion, we have proposed and demonstrated a conformal dual-band antenna with a compact footprint, light-weight, and low-profile design for wearable applications. A miniaturized slotted JC metallic sheet backed isotropic metasurface was employed to provide capacitive loading, which enables impedance to match the inductive feed element in the Wireless WLAN band of $5.15 \sim 5.25$ GHz and $5.72 \sim 5.83$ GHz. The realized antenna accomplishes a 4.07% -10 dB bandwidth at $5.06 \sim 5.27$ GHz, a 4.16% -10 dB bandwidth at $5.60 \sim 5.84$ GHz, and a gain around 8 dB at the two bands. The SAR simulations further prove the superiority of the proposed antenna, showing a low SAR value and robust performance to human body loading. Therefore, the proposed integrated metasurface-enabled antenna will be a good candidate for wearable device in terms of bandwidth, efficiency, SAR and stability.

ACKNOWLEDGMENT

This work was supported by the National Natural Science Foundation of China (No. 41474117) and by self-determined research funds of Central China Normal University from the Colleges' Basic Research and Operation of Ministry of Education of China (No. CCNU15GF005).

REFERENCES

1. Alomainy, A., H. Yang, A. Owadally, C. G. Parini, Y. Nechayev, and C. C. Constantinou, "Statistical analysis and performance evaluation for on-body radio propagation with microstrip patch antennas," *IEEE Transactions on Antennas and Propagation*, Vol. 55, No. 1, 245–248, 2007.
2. Hall, P. S., H. Yang, Y. I. Nechayev, A. Alomainy, C. C. Constantinou, and C. Parini, "Antennas and propagation for on-body communication systems," *IEEE Antennas and Propagation Magazine*, Vol. 49, No. 3, 41–58, 2007.
3. Hertleer, C., A. VanLaere, H. Rogier, and L. van Langenhove, "Influence of relative humidity on textile antenna performance," *Textile Research Journal*, Vol. 80, No. 2, 177–183, 2009.
4. Osman, M. A. R., M. K. Abd Rahim, N. A. Samsuri, H. A. M. Salim, and M. F. Ali, "Embroidered fully textile wearable antenna for medical monitoring applications," *Progress In Electromagnetics Research*, Vol. 117, 321–337, 2011.
5. Kurup, D., W. Joseph, G. Vermeeren, and L. Martens, "Specific absorption rate and path loss in specific body location in heterogeneous human model," *IET Microwaves, Antennas & Propagation*, Vol. 7, No. 1, 35–43, 2013.
6. Nechayev, Y. I., X. Wu, C. C. Constantinou, and P. S. Hall, "Millimetre-wave path-loss variability between two body-mounted monopole antennas," *IET Microwaves, Antennas & Propagation*, Vol. 7, No. 1, 1–7, 2013.
7. Bai, Q. and R. Langley, "Crumpling of PIFA textile antenna," *IEEE Transactions on Antennas and Propagation*, Vol. 60, No. 1, 63–70, 2012.
8. Soh, P. J., G. A. E. Vandenbosch, O. S. Liam, and N. H. M. Rais, "Design of a broadband all-textile slotted PIFA," *IEEE Transactions on Antennas and Propagation*, Vol. 60, No. 1, 379–384, 2012.
9. Geng, J.-P., J. Li, R.-H. Jin, S. Ye, X. Liang, and M. Li, "The development of curved microstrip antenna with defected ground structure," *Progress In Electromagnetics Research*, Vol. 98, 53–73, 2009.
10. Shao, Z. Z. and R. Langley, "Dual-band wearable textile antenna on an EBG substrate," *IEEE Transactions on Antennas and Propagation*, Vol. 57, No. 4, 926–935, 2009.

11. Koschny, T., M. Kafesaki, E. N. Economou, and C. M. Soukoulis, "Effective medium theory of left-handed materials," *Physical Review Letters*, Vol. 93, No. 10, 107402, 2004.
12. Schurig, D., J. Mock, and D. Smith, "Electric-field-coupled resonators for negative permittivity metamaterials," *Applied Physics Letters*, Vol. 88, No. 4, 041109, 2006.
13. Gay-Balmaz, P. and O. J. Martin, "Electromagnetic resonances in individual and coupled split-ring resonators," *Journal of Applied Physics*, Vol. 92, No. 5, 2929–2936, 2002.
14. Nanfang, Y., P. Genevet, M. A. Kats, F. Aieta, J. Tetienne, F. Capasso, and Z. Gaburro, "Light propagation with phase discontinuities: Generalized laws of reflection and refraction," *Science*, Vol. 334, No. 6054, 333–337, 2011.
15. Zhu, H., S. W. Cheung, K. L. Chung, and T. I. Yuk, "Linear-to-circular polarization conversion using metasurface," *IEEE Transactions on Antennas and Propagation*, Vol. 61, No. 9, 4615–4623, 2013.
16. Dickie, R., R. Cahill, N. Mitchell, H. Gamble, and V. Fusco, "664 GHz dual polarisation frequency selective surface," *Electronics Letters*, Vol. 46, No. 7, 472–474, 2010.
17. Vallecchi, A., J. R. De Luis, F. Capolino, and F. D. Flaviis, "Low profile fully planar folded dipole antenna on a high impedance surface," *IEEE Transactions on Antennas and Propagation*, Vol. 60, No. 1, 51–62, 2012.
18. Sievenpiper, D., L. Zhang, R. F. J. Broas, N. G. Alexopolous, and E. Yablonovitch, "High-impedance electromagnetic surfaces with a forbidden frequency band," *IEEE Transactions on Microwave Theory and Techniques*, Vol. 47, No. 11, 2059–2074, 1999.
19. Simovski, C. R., P. de Maagt, and I. V. Melchakova, "High-impedance surfaces having stable resonance with respect to polarization and incidence angle," *IEEE Transactions on Antennas and Propagation*, Vol. 53, No. 3, 908–914, 2005.
20. Kundu, A. and A. K. Bhattacharjee, "Design of compact triple frequency microstrip antenna for WLAN/WiMAX applications," *Microwave and Optical Technology Letters*, Vol. 57, No. 9, 2125–2129, 2015.
21. Burokur, S. N., J. P. Daniel, P. Ratajczak, and A. de Lustrac, "Tunable bilayered metasurface for frequency reconfigurable directive emissions," *Applied Physics Letters*, Vol. 97, No. 6, 064101, 2010.
22. Wakatsuchi, H., S. Kim, J. J. Rushton, and D. F. Sievenpiper, "Circuit-based nonlinear metasurface absorbers for high power surface currents," *Applied Physics Letters*, Vol. 102, No. 21, 214103, 2013.
23. Yuandan, D. and T. Itoh, "Metamaterial-based antennas," *Proceedings of the IEEE*, Vol. 100, No. 7, 2271–2285, 2012.
24. Liu, Y. and X. Zhang, "Metamaterials: A new frontier of science and technology," *Chemical Society Reviews*, Vol. 40, No. 5, 2494–2507, 2011.
25. Jiang, Z., D. E. Brocker, P. E. Sieber, and D. H. Werner, "A compact, low-profile metasurface-enabled antenna for wearable medical body-area network devices," *IEEE Transactions on Antennas and Propagation*, Vol. 62, No. 8, 4021–4030, 2014.
26. Ziolkowski, R. W., P. Jin, and C.-C. Lin, "Metamaterial-inspired engineering of antennas," *Proceedings of the IEEE*, Vol. 99, No. 10, 1720–1731, 2011.
27. Raad, H. R., A. I. Abbosh, H. M. Al-Rizzo, and D. G. Rucker, "Flexible and compact AMC based antenna for telemedicine applications," *IEEE Transactions on Antennas and Propagation*, Vol. 61, No. 2, 524–531, 2013.
28. Jiang, Z. and D. H. Werner, "Robust low-profile metasurface-enabled wearable antennas for off-body communications," *2014 8th European Conference on Antennas and Propagation (EuCAP)*, April 2014.
29. Cahill, R. and E. A. Parker, "Concentric ring and Jerusalem cross arrays as frequency selective surfaces for a 45Â° incidence diplexer," *Electronics Letters*, Vol. 18, No. 8, 313–314, 1982.
30. Stuchly, M. and S. Stuchly, "Dielectric properties of biological substances-tabulated," *Journal of Microwave Power*, Vol. 15, No. 1, 19–26, 1980.